Hindawi
IET Electrical Systems in Transportation
Volume 2024, Article ID 2889871, 19 pages
https://doi.org/10.1049/2024/2889871

Research Article

The Impact of Wheel Flat on Traction Drive System of Electric Locomotives

Like Pan[1], **Bing Lu**[2], **Caizhi Yang**[1], **Liming Chen**[1], **Yang Song**[2,3] and **Tao Zhang**[4]

[1]*Standards and Metrology Research Institute, China Academy of Railway Sciences Corporation Limited, Beijing 100081, China*
[2]*National Rail Transit Electrification and Automation Engineering Technique Research Centre, Southwest Jiaotong University, Chengdu 610031, China*
[3]*State Key Laborotary of Rail Transit Vehicle System, Southwest Jiaotong University, Chengdu 610031, China*
[4]*Equipment Technology Center, National Railway Administration of P. R. China, Beijing 100860, China*

Correspondence should be addressed to Liming Chen; 13810305638@163.com and Yang Song; y.song_ac@hotmail.com

Received 2 December 2023; Revised 19 March 2024; Accepted 28 March 2024; Published 16 April 2024

Academic Editor: Lei Chu

Wheel flat can seriously affect the wheel–rail contact performance and cause impact vibrations, which significantly threaten the safe operation of railway vehicles. It is crucial to accurately assess the effects of wheel flats on the wheel–rail contact performance and the vibration impact on the traction drive system. However, studies related to wheel flats have focused on the mechanical part and have yet to fully consider the electrical and mechanical parts of the entire traction drive system. Therefore, this paper first builds an electromechanical coupling model based on the electric traction drive system and the locomotive-track coupling dynamics model. Then, based on this model, the impact of the wheel flat on the electrical and mechanical parts of the traction drive system under different flat lengths, different flat depths, and different vehicle speeds was analyzed. The results indicate that with the increasing depth of the flat spot, the wheel–rail dynamic response, motor rotor speed, and motor torque exhibit more significant fluctuations. Additionally, as the locomotive speed increases, the impact of the flat on the wheel–rail contact performance intensifies. Wheel flats can excite the 1st bending mode of the wheelset, resulting in vibration shocks at 90 Hz.

1. Introduction

The dynamic interaction between vehicles and tracks has intensified with the increase in train operating speeds and axle loads. As a result, the service environment for the wheels has deteriorated, leading to more severe wear and damage between the wheels and the track [1–3]. Currently, wheel flat is one form of wheel wear in railway vehicles. Wheel flats refer to the damage caused by wheel sliding during conditions such as startup and braking when the wheels lock or experience low adhesion [4, 5], as shown in Figure 1. Wheel flats can lead to significant impact loads and seriously reduce the service life of the wheels [5]. In extreme cases, wheel flats can even cause derailment, posing a significant threat to the safety of railway vehicle operations. Hence, an accurate analysis of the impact of wheel flat on wheel–rail contact parameters and the drive system is urgently needed. In addition, accurate detection of wheel flat scars is also crucial. The automatic damage identification algorithm proposed by Mosleh et al. [6, 7] can be used to detect wheel tread damage.

Domestic and international scholars have conducted extensive research on the wheel–rail impact issue caused by wheel flats through experimental research, theoretical research, and numerical simulation. Existing research mainly focuses on the influence of wheel flat scars on wheel–rail impact force, vehicle-rail system dynamics, and transmission system vibration.

1.1. Wheel–Rail Impact Force. Wheel flat can directly cause a large vertical relative displacement between the wheel and the rail, resulting in a considerable impact. In [8], a simplified formula for calculating impact force was introduced based on the formula relating low joint impact force and flat impact velocity. Uzzal et al. [9, 10] researched the characteristics of wheel–rail impact forces caused by individual wheel flats and multiple wheel flats and analyzed the impact of train speed, flat length, and vehicle suspension parameters

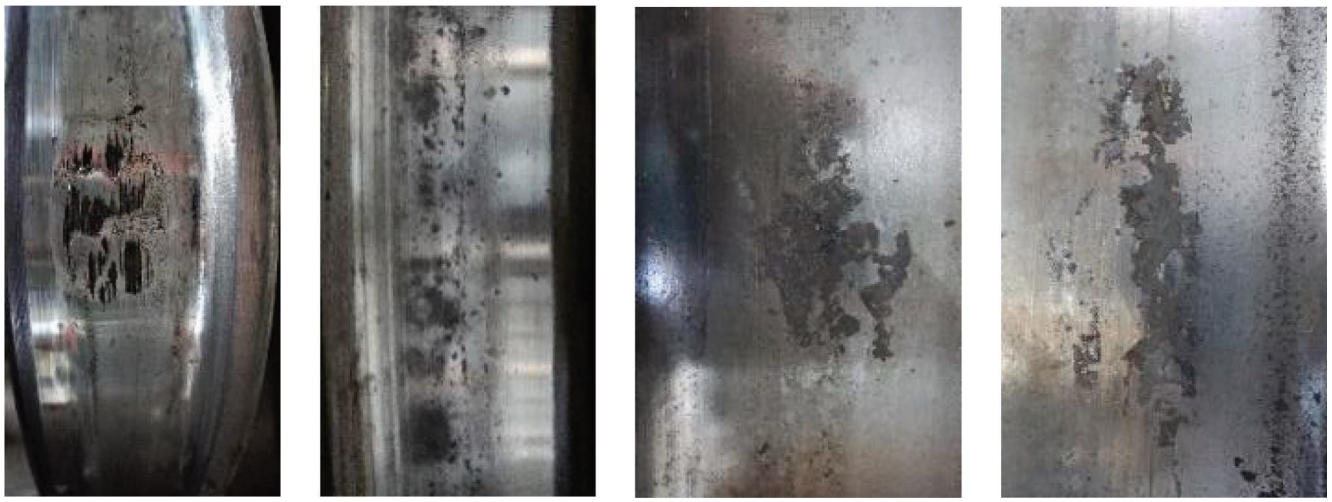

Figure 1: Wheel flat.

on the wheel–rail forces. In [11], a non-Hertzian foundational theoretical model was established considering the actual dimensions of wheel flats, and the vibration impact caused by wheel flats was analyzed. Similarly, Baeza et al. [12] studied the wheel–rail impact force caused by wheel flats, considering both new and worn wheel flats using a non-Hertzian contact theory. The research findings indicate that within the 20–200 km/hr speed range, the maximum wheel–rail impact force caused by new wheel flats increases with increasing train speed. However, the rate of increase gradually diminishes. It is worth noting that in [13], a full-scale high-speed wheel–rail interface test rig was used to test the wheel–rail dynamic impact caused by the wheel flat, and the same conclusion was obtained. In [14], wheel flats were input into the wheel-rail system as uneven displacements at the wheel–rail interface, and the impact and vibration characteristics caused by wheel flats were studied.

1.2. Vehicle-Track System Dynamics. The severe impact between the wheel and rail caused by the wheel flat can be transmitted to the entire vehicle-track coupling dynamic system. Lin et al. [15] established a rigid-flexible coupled model of high-speed trains and a finite element model for flat damage contact. The impact of single- or double-wheel flats with different positional distributions on the wheel–rail dynamics was analyzed [15]. In [16], the dynamic characteristics of the wheel–rail interaction under the influence of new and worn wheel flats in heavy freight trains were studied based on the vehicle-track coupled dynamics theory, and suggestions for the maximum allowable limits of the two types of wheel flats were proposed. Han et al. [17] conducted numerical simulations using a finite element explicit algorithm and considered the strain rate-related parameters of wheel–rail materials to investigate the wheel–rail impact response caused by wheel flats in high-speed trains. In [18, 19], a 3D wheel flat model considering length, width, and depth was established, and the influence of wheel flat on the dynamic response of the vehicle-track system was analyzed. Wang et al. [20] found that wheel flats caused a significant increase in contact force, contact stress, frictional force, and vibration acceleration between the brake interfaces. Additionally, Ye et al.'s [21] research showed that wheel flats can cause or exacerbate wheel polygonal wear, and the vehicle operating speed and the length of the flats significantly impact wheel polygonal wear.

1.3. Vibration of the Traction Drive System. Yang et al. [22] developed a wheel–rail dynamics model equipped with a gear system and analyzed the time-domain and frequency-domain effects of wheel flats on the gear system under variable speed conditions. The study conducted by Wang et al. [23] found that wheel flats can cause high-frequency vibrations in longitudinal creep forces and gear mesh forces. Similarly, a vehicle-track dynamics model considering the dynamic coupling of the gear system was established, and the effects of wheel flats on wheel–rail forces and gear mesh forces were analyzed [24]. The vibration impact of wheel flats on motor bearings was analyzed by combining the Miner linear damage theory and vehicle-track coupled dynamics [25]. The results showed that the periodic impact forces and high contact forces caused by wheel flats would reduce the fatigue life of the motor. The study in [26] demonstrated that wheels with flats exhibit more pronounced dynamic characteristics under traction and braking conditions, while the characteristic changes under sliding conditions are not significant.

In summary, there have been many studies on wheel flat, as shown in Table 1. However, these studies have mainly focused on the mechanical aspects of the traction drive system. A complete traction drive system consists of rectifiers, inverters, motors, gearboxes, and wheelsets. The traction drive system is a complex electromechanical coupling model where the vibration impact caused by wheel flats can be propagated to the electrical components of the drive system. Additionally, the fluctuating torque output by the traction motor can exacerbate the dynamic response fluctuations of the wheel–rail system [3]. Therefore, relying solely on mechanical vibrations is insufficient to accurately calculate the dynamic response of the wheel–rail system and the traction drive system. In order to address this issue, this study

Table 1: Classification of wheel flat research.

Categories	References	Research focuses
Wheel–rail impact force caused by wheel flat	[8]	Calculating the wheel–rail impact force and impact velocity
	[9–14]	The influence of flat length, depth, and vehicle speed on wheel–rail impact force
The influence of wheel flat on the vehicle-track system dynamics	[15–20]	The influence of flat on wheel–rail contact response
	[21]	The influence of flat on wheel wear
The influence of wheel flat on traction drive system	[22–24]	The influence of flat on gear system
	[25]	The influence of flat on traction motor
	[26]	The influence of flat on wheel–rail impact under traction and braking conditions

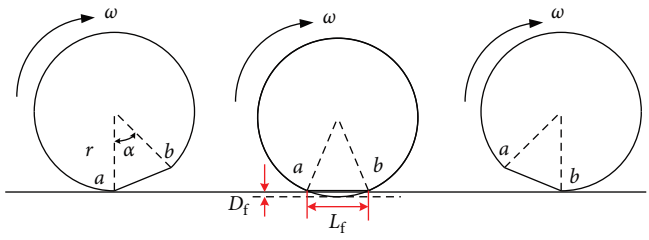

Figure 2: The motion characteristics of a wheel with flats at low speeds.

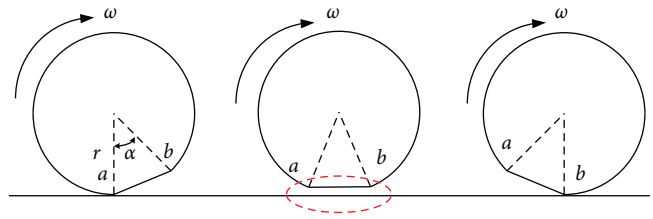

Figure 3: The motion characteristics of a wheel with flats at high speeds.

employs an electromechanical coupling model to analyze the impact of wheel flats on both the electrical and mechanical aspects of the traction drive system.

The main contributions of this study are as follows: Considering the electromechanical coupling effect of the traction transmission system, a comprehensive analysis is conducted on the vibration impact of flat length, flat depth, and operating speed on the local dynamic response of the wheel–rail system. In addition, the influence of wheel flat scars on the electrical side rotor speed and motor torque fluctuations is also investigated.

2. Wheel Flat Impact Theory

In this section, it is assumed that the rail is rigid. In the case of an ideal wheel, the distance between the wheel center and the wheel–rail contact point is equal to the wheel radius. When analyzing the motion of a wheel with flats, it can be divided into low-speed and high-speed conditions [4].

In the low-speed scenario, depicted in Figure 2, the wheel undergoes a specific behavior as it rolls to point "*a*." It rotates around point "*a*" until the entire flat surface of the wheel aligns with the rail surface. At this juncture, the drop in the wheel center matches the depth of the flat spot, and point "*b*" of the wheel exerts a notable impact on the rail. Following this, the wheel rotates around point "*b*," ultimately restoring its normal rolling state.

In the high-speed scenario, as shown in Figure 3, after the wheel rolls to point "*a*," wheel–rail separation occurs. At this juncture, the normal force between the wheel and rail becomes zero. The wheel center undergoes a parabolic motion with a horizontal initial velocity of v under the effect of the wheel's self-weight and axle load. Eventually, the wheel's point "*b*" imparts a greater impact on the rail.

From the above analysis, it can be concluded that the impact characteristics of the wheel flat will inevitably change at a certain critical impact speed. The time for the wheel to rotate around point "*a*" by an angle $\alpha/2$ is denoted as t_1. The height corresponding to the wheel flat length is h. The time for the wheel center to drop h is denoted as t_2. Assuming that the critical speed is v_0, which should satisfy $t_1 = t_2$. t_1 and t_2 can be calculated respectively as follows [4]:

$$t_1 = \alpha/(2\omega), \tag{1}$$

$$t_2 = \sqrt{2h/a_0}, \tag{2}$$

where ω is the wheel rolling angular velocity, a_0 is the wheel drop acceleration in vertical direction. According Newton's second law, a_0 can be presented as follows:

$$a_0 = \left(F_{pszL} + F_{pszR} + m_2 g\right)/m_2, \tag{3}$$

where F_{pszL} is the vertical force of primary spring on the left side of the wheelset; F_{pszR} is the vertical force of primary spring on the right side of the wheelset; m_2 denotes the primary unsprung mass of the wheelset; g is the acceleration due to gravity. According to the theory of multibody dynamics for locomotives, the vertical force exerted by primary springs can be expressed as the sum of the gravitational force corresponding to the primary unsprung mass and the prestress of primary sprung, which can be written as follows:

$$F_{psz} = m_1 g + F_{pre}, \tag{4}$$

where F_{spz} is the superposition of F_{spzL} and F_{spzR}; m_1 denotes the primary sprung mass of the wheelset; F_{pre} is prestress of primary sprung.

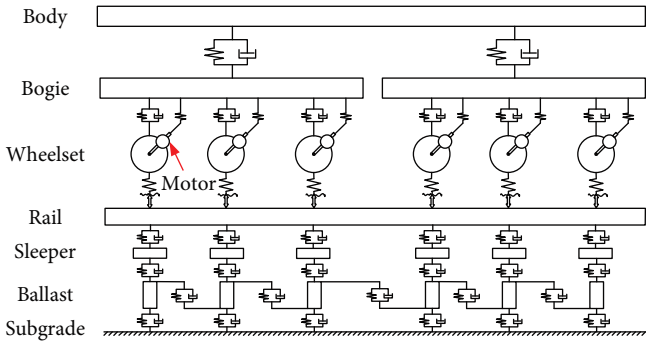

Figure 4: Locomotive-track coupling dynamics model.

When $t_1 = t_2$, thus

$$\frac{\alpha}{2\omega} = \frac{\alpha r}{2v} = \sqrt{\frac{2hm_2}{(F_{psz} + m_2)g}}. \tag{5}$$

Let $h = r(1 - \cos\frac{\alpha}{2}) \approx \frac{1}{8}r\alpha^2$, critical speed v_0 can be expressed as follows:

$$v_0 = \sqrt{\frac{F_{psz} + m_2 g}{m_2}}\, r, \tag{6}$$

where r is the radius of the wheel. According to Zhai [27], when the vehicle speed is less than the critical speed, the wheel impact speed can be calculated as follows:

$$v_{max} = (1 + \gamma)\frac{L_f}{2r}v, \tag{7}$$

where γ is the coefficient for converting the rotational inertia of wheels into reciprocating inertia, L_f is the length of the wheel flat. When the vehicle speed is larger than the critical speed, the wheel impact speed can be calculated as follows:

$$v_{max} = \frac{L_f}{v + \sqrt{a_0 r}}\left(a_0 + \gamma v\sqrt{\frac{a_0}{r}}\right). \tag{8}$$

3. Electromechanical Coupling Model

3.1. Locomotive-Track Coupling Dynamics Model. The locomotive-track coupled dynamics model mainly consists of three parts: the locomotive dynamics model, the track subsystem model, and the wheel–rail coupling subsystem model, as shown in Figure 4. Based on the vehicle dynamics theory [24, 28] and the actual locomotive parameters listed in Table 2, a detailed locomotive dynamics model is established in SIMPACK. The model includes one body, two bogies, six wheelsets, and six motors. The motor suspension in this locomotive is axle-hung, so only the vertical and pitch degrees of freedom of the motors are considered, while the other components are considered to have 6 degrees of freedom. The wheelsets are treated as flexible bodies, and their modal analysis results are shown in Figure 5. In

Table 2: Parameters of the vehicle system.

Parameter	Value
Car body mass (kg)	6.26×10^4
Bogie mass (kg)	7.84×10^3
Wheelset mass (kg)	2.77×10^3
Motor mass (kg)	2.66×10^3
Mass moment of inertia of car body (kg · m^2)	1.434×10^6
Mass moment of inertia of bogie frame (kg · m^2)	1.311×10^4
Mass moment of inertia of wheelset (kg · m^2)	4.2×10^2
Mass moment of inertia of motor (kg · m^2)	2×10^2
Stiffness of primary suspension (N/m)	3.14×10^6
Stiffness of secondary suspension (N/m)	2.14×10^6
Stiffness of suspension connecting motor and bogie frame (N/m)	1.0×10^{10}
Stiffness of axle-hung bearing supporting motor on wheel axle (N/m)	1.0×10^{10}
Damping coefficient of primary suspension (N s/m)	5×10^4
Damping coefficient of suspension connecting motor and bogie frame (N s/m)	9×10^4
Damping coefficient of secondary suspension (N s/m)	1.0×10^3
Damping coefficient of axle-hung bearing supporting motor on wheel axle (N s/m)	1.0×10^3
Semi-longitudinal distance between bogies (m)	5.03
Semi-longitudinal distance between wheelsets in bogie (m)	1.3
The longitudinal distance between bogie center and hung position of motor on bogie (m)	0.374
Longitudinal distance between pinion center and hung position of motor on bogie (m)	0.35
Distance between centers of pinion and gear (m)	0.576
Wheel radius (m)	0.625

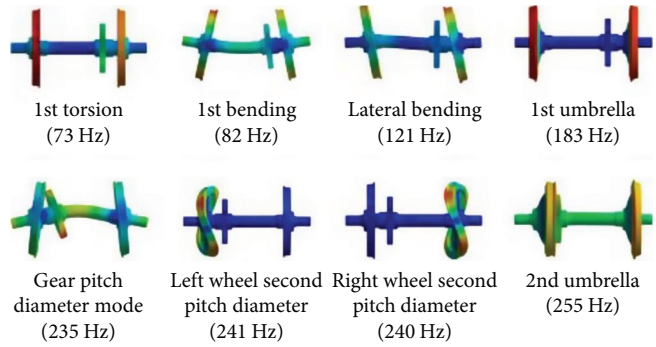

Figure 5: Modal analysis results of flexible wheelset.

the modal analysis of the wheelset, it is assumed that the wheel and gear are rigidly attached to the axle without considering their relative motion. An 8-node and 6-hexahedral element discretization is employed for the wheelset. The wheelset is assumed to have free boundary conditions, and the Lanczos method is used to calculate its modal characteristics. Figure 5 shows the mode shapes and natural frequencies of the first 8-order modes of the flexible wheelset. As the wheel flat mainly induces vertical vibration impacts between the wheel and rail, the first bending mode may be excited, resulting the presence

Table 3: Parameters of track system.

Parameter	Value
Elastic modulus of rail (N/m^2)	2.0591×10^{11}
Torsional inertia of rail (m^4)	3.741×10^{-5}
Rail second moment of area about Y-axis (m^4)	3.217×10^{-5}
Rail second moment of area about Z-axis (m^4)	5.24×10^{-6}
Rail torsional stiffness (N m/rad)	1.9587×10^{5}
Rail mass per unit length (kg/m)	60.64
Density of rail (kg/m^3)	7.86×10^{3}
Sleeper spacing (m)	0.545
Effective support length of half half-sleeper (m)	1.25
Sleeper width (m)	0.273
Ballast mass (kg)	660
Ballast density (kg/m^3)	1.75×10^{3}
Ballast stiffness (N/m)	1.5×10^{7}
Ballast damping (N·s/m)	5.88×10^{4}
Elastic modulus of ballast (Pa)	1.2×10^{7}

of vertical oscillation components around 82 Hz in the wheel–rail contact parameters.

The track system model is simplified as a double-mass (rail pad and sleeper), three-layer (rail-sleeper-ballast) spring-damping model; the detailed modeling parameters are shown in Table 3. Equivalent spring-damping units are used to connect these components of the track system. The accuracy of the vehicle-track coupling dynamics model has been verified in the authors' previous work [3]. The wheel–rail coupling subsystem mainly consists of the normal contact and tangential contact models. The Hertz contact theory is used to simulate the normal contact for the wheel–rail system [29], while the FASTSIM algorithm is responsible for the tangential contact [30–32].

The primary function of this subsystem is to calculate the wheel-rail normal forces, creep forces, and size of the contact patch. In the Hertz contact theory, the contact patch between the wheel and rail is equivalent to an ellipse and can be represented as follows [29]:

$$\begin{cases} a = m\left[\dfrac{3}{4}\times\dfrac{G^*}{A+B}P\right] \\ b = n\left[\dfrac{3}{4}\times\dfrac{G^*}{A+B}P\right] \end{cases}, \tag{9}$$

where a and b denote the long half-axis and short half-axis of the ellipse, respectively, A and B denote longitudinal and lateral relative curvature; P denotes wheel-rail normal force; G^* is determined by the materials of the wheel and rail, and can be represented as follows:

$$G^* = \frac{1-\nu_w^2}{E_w} + \frac{1-\nu_r^2}{E_r}, \tag{10}$$

where ν_r and E_r are Poisson's ratio and elastic modulus of rail material, respectively, ν_w and E_w are Poisson's ratio and elastic modulus of wheel material, respectively. The main function of Hertzian theory is to solve the distribution of normal force, which can be expressed as follows [31]:

$$p_v(x,y) = \frac{3P}{2\pi ab}\sqrt{1-\left(\frac{x}{a}\right)^2-\left(\frac{y}{b}\right)^2}. \tag{11}$$

Wheel-rail creepage is an important parameter for evaluating wheel-rail contact performance. According to Yang et al. [22], when the wheel-rail contact is in a full sliding state, the calculation of the wheel-rail creepage needs to consider the relative vibration speed between the wheel and the rail. The wheel-rail creep force can be expressed as follows:

$$F_c = P\times\mu, \tag{12}$$

where μ denotes the friction coefficient between the wheel and rail, which can be calculated as follows:

$$\mu = a_\mu e^{-x_\mu v_{slip}} - b_\mu e^{-y_\mu v_{slip}}, \tag{13}$$

where $a_\mu, b_\mu, x_\mu, y_\mu$ are the key parameters that affect the friction coefficient. v_{slip} represents the relative slip speed between wheel and rail, which can be calculated by wheel angular velocity ω and vehicle forward velocity v. Thus, relative slip speed v_{slip} can be expressed as follows [33]:

$$v_{slip} = \omega r - v, \tag{14}$$

where r is the wheel radius.

The main objective of this paper is to investigate the impact of wheel flats on the vibration of the traction drive system. Therefore, it is necessary to incorporate the initial defect of the wheel into the locomotive-track coupling dynamics model. According to Li et al. [34], the wheel flat can be described using a cosine function, which can be represented as follows:

$$r(x) = \frac{1}{2}D_f\left[1-\cos\left(\frac{2\pi x}{L_f}\right)\right], \tag{15}$$

where D_f is the depth of the wheel flat, L_f is the length of the wheel flat. The relationship between the length and depth of wheel flat can be expressed as follows:

$$D_f = \frac{L_f^2}{16r}. \tag{16}$$

3.2. Electric Traction Drive System. The electric traction drive system, as the power source for locomotive operation [35–38], mainly consists of rectifiers, DC links, inverters, and traction motors [39–42], as shown in Figure 6. Single-phase 25 kV AC power from the traction grid is converted to DC 1,800 V power through the rectifier [43–45]. In this system, the speed control method for the motor is variable frequency control [46–48]. Therefore, the DC power is converted to three-phase AC power with variable amplitude and

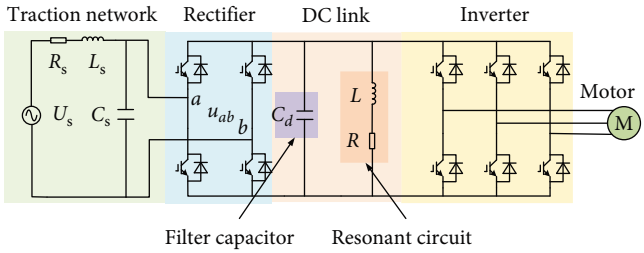

Figure 6: Electrical traction drive system.

Table 4: Modeling parameters of electric traction drive system.

Parameters	Value
Rated frequency (Hz)	66.6
Number of pole pairs	2
Stator resistance (mΩ)	18.5
Stator leakage inductance (mH)	0.198
Rotor resistance (mΩ)	18.5
Rotor leakage inductance (mH)	0.198
Mutual inductance (mH)	7.75

frequency through the inverter, which is then supplied to the asynchronous motor. A Simulink model of the electric traction system is constructed, with specific modeling parameters shown in Table 4. The rectifier adopts transient current control [49, 50], while the inverter-motor system uses indirect field-oriented vector control [41, 51, 52].

3.3. Coupling of Electrical and Mechanical Parts of Traction Drive System. The traction motor converts electrical energy from the electric traction drive system into mechanical energy in the form of electromagnetic torque, which is then transmitted to the gearbox to drive the wheels and propel the vehicle [53, 54]. Therefore, the traction motor itself is an electromechanical coupling module. By establishing a closed-loop feedback between the electric traction drive system model in Simulink and the locomotive-track coupled dynamics model in SIMPACK, the electrical side and mechanical side of the drive system are coupled together. Specifically, the torque output from the motor in Simulink is applied to the motor shaft in SIMPACK, while the rotor speed output from SIMPACK is fed back to the motor control system in Simulink. The transfer of these parameters is facilitated through the interface SIMAT between Simulink and SIMPACK, ensuring real-time interaction and closed-loop feedback between the electrical and mechanical systems, as shown in Figure 7.

4. Analysis of Simulation Results

From the locomotive wheel out-of-roundness experiments, it is known that wheel flats exhibit various patterns. In order to fully investigate the impact of wheel flats on the traction drive system, this paper adopts a controlled variable method to consider the effects of different lengths and depths of flats. Additionally, this study takes into account the impact of wheel flats on the drive system under different locomotive operating speeds. Specifically, three simulations are conducted:

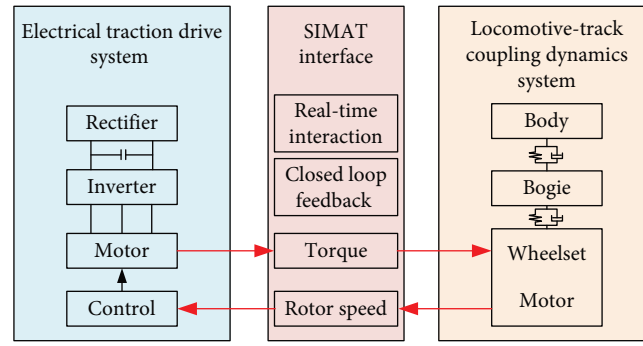

Figure 7: Diagram of the electromechanical coupling model.

Test 1: The locomotive operates at a speed of 70 km/hr, with a flat depth of 0.24 mm. The range of the flat lengths is from 0.05 to 0.35 m, with an interval of 0.1 m, as shown in Figure 8(a).

Test 2: The locomotive operates at a speed of 70 km/hr, with a flat length of 0.25 m. The range of flat depths is from 0.18 to 0.36 mm, with an interval of 0.06 mm, as shown in Figure 8(b).

Test 3: The flat length is 0.25 m, and the flat depth is 0.24 mm. The locomotive operates at a speed range of 60–100 km/hr.

4.1. The Impact of Wheel Flat Depth on Traction Drive System. According to the simulation settings in Test 1, the electromechanical coupling model established in Section 3 is operated. Due to the presence of initial wheel defects (flats), there will be instability in the locomotive-track coupled dynamics during the initial stage of operation. Therefore, the dynamic model undergoes free uniform linear motion from 0 to 10 s. After 10 s, the mechanical and electrical parts of the traction drive system are coupled. It is worth noting that this approach is employed for all subsequent simulations in this paper. Key data from the electrical and mechanical sides of the traction drive system are obtained, such as the wheel-rail normal force, creepage ratio, contact patch characteristics, rotor speed, and torque, as shown in Figures 9–16.

From Figure 9(a), it can be observed that as the flat depth increases, there is an increasing fluctuation in the wheel-rail normal force. Figure 10 shows the wheel-rail normal force with and without torque excitation. When the wheel rolls over the flat, there is a significant impact between the wheel and the rail, which then gradually attenuates. Comparing Figures 10(a) and 10(b), it can be seen that without torque excitation, the wheel-rail normal force essentially attenuates to a stable state. However, in the presence of torque excitation, the normal force first attenuates and then continues to exhibit small-amplitude oscillations. The fast Fourier transform (FFT) [55] analysis of the normal force reveals that the main fluctuation frequency is 90 Hz, which is attributed to the vibration impact caused by the wheel flat exciting the first bending mode of the flexible wheel (as seen in Figure 5).

The longitudinal creepage, lateral creepage, and spin creepage between the wheel and rail are shown in Figures 11–13,

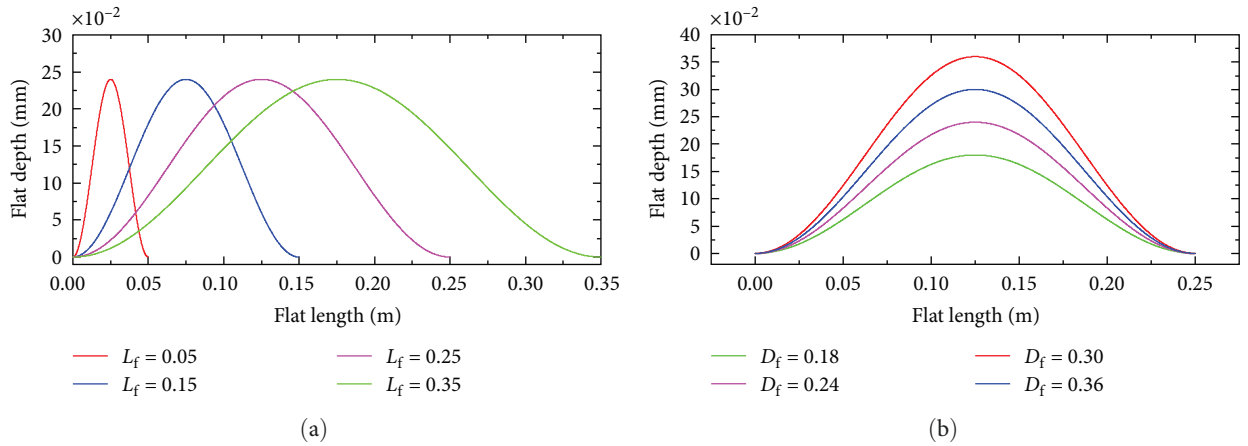

Figure 8: Diagram of wheel flat: (a) $L_f = 0.05$–0.35 m, $D_f = 0.08$ mm; (b) $D_f = 0.18$–0.36 mm, $L_f = 0.25$ m.

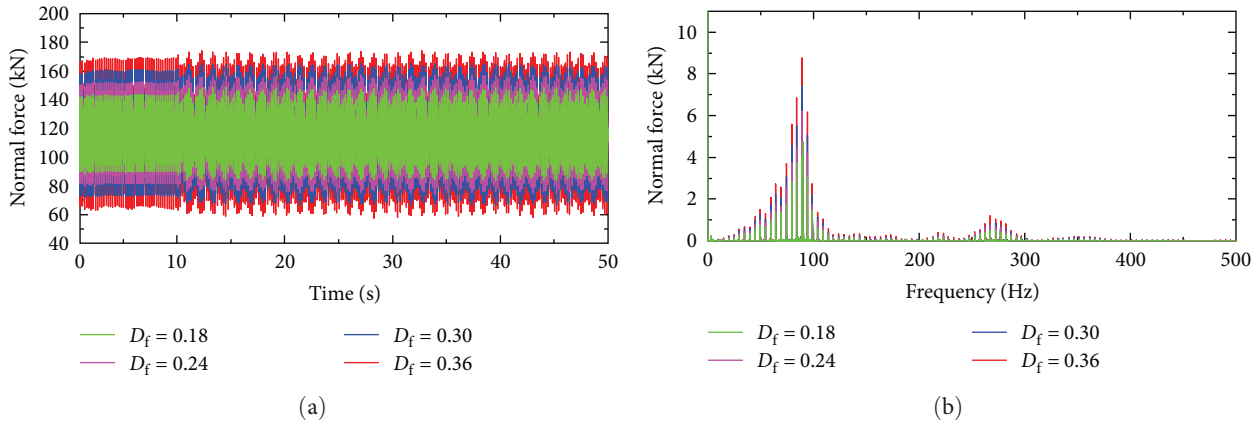

Figure 9: Wheel-rail normal force: (a) time history; (b) FFT analysis.

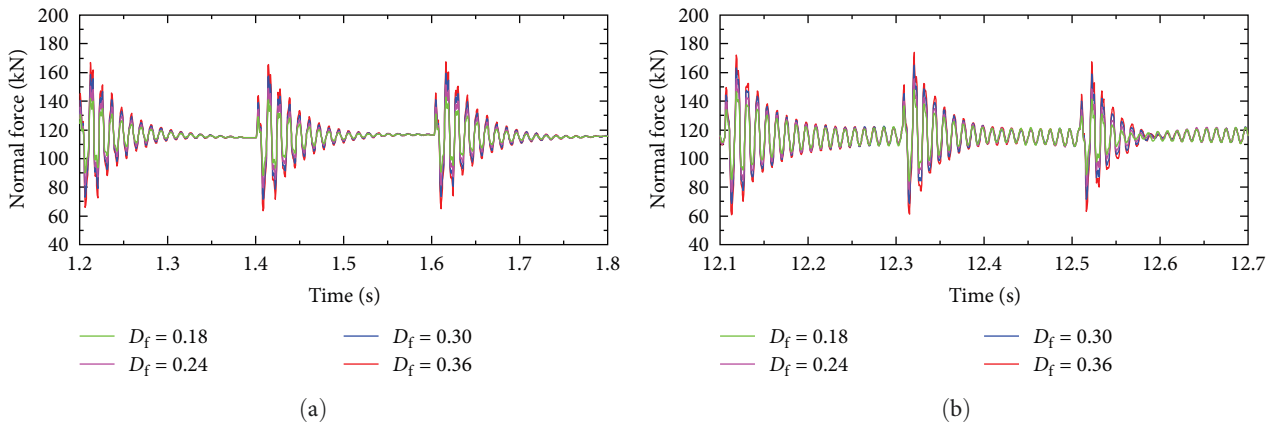

Figure 10: Magnified view of wheel normal force: (a) 1.2–1.8 s; (b) 12.1–12.7 s.

respectively. As the depth of the wheel flat increases, the fluctuations in wheel-rail creepage in all directions also increase. The frequency of these creepage fluctuations is concentrated at 90 Hz. The average value of the longitudinal creepage shown in Figure 11 increases after 10 s, which is attributed to the traction torque driving the wheels, resulting in an increase in the relative slip between the wheel and rail.

Figure 14 illustrates the size of the contact patch between the wheel and rail. It can be observed that an increase in the depth of the wheel flat leads to a larger contact patch. This result corresponds to the wheel-rail normal force shown in Figure 9. Due to the wheel-rail vibration impact caused by the flat, when the normal force reaches the peak value, the size of the contact patch between the wheel and rail also

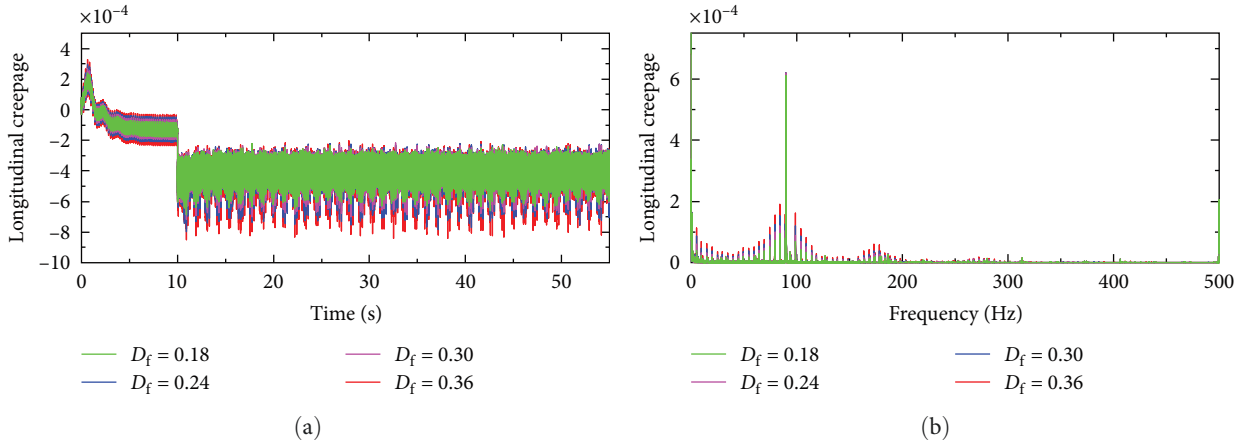

Figure 11: Longitudinal creepage: (a) time history; (b) FFT analysis.

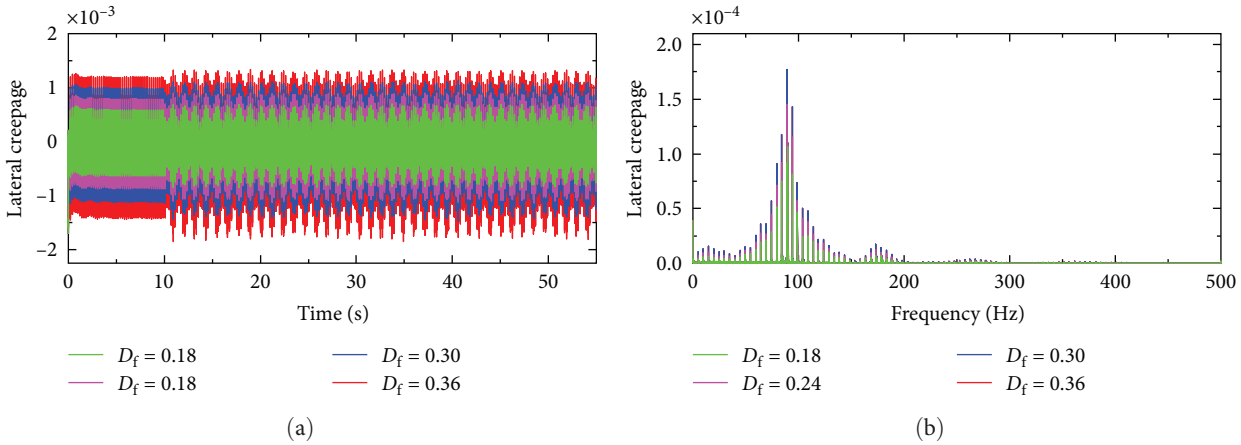

Figure 12: Lateral creepage: (a) time history; (b) FFT analysis.

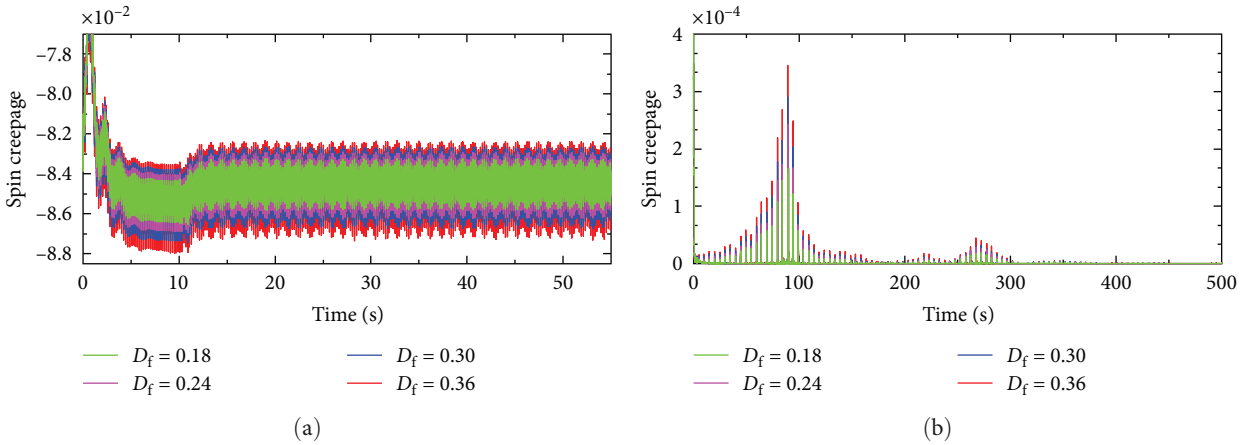

Figure 13: Spin creepage: (a) time history; (b) FFT analysis.

reaches the peak value. Accordingly, the frequency of the contact patch size fluctuations aligns with that of the normal force.

Figure 15 presents the rotor angular velocity of the motor. It can be observed that variations in the depth of the wheel flat have a relatively small impact on the fluctuation of the rotor speed. When the depth of the flat increases, there is a slight increase in the fluctuation of the rotor speed. From Figure 15(b), it can be seen that the frequency of the rotor speed fluctuations is also around 90 Hz. Comparing the dynamic parameters shown in Figures 9–15, it can be concluded that the vibration impact caused by the wheel flat primarily manifests in the vertical direction and has a relatively minor influence on the rotor rotation.

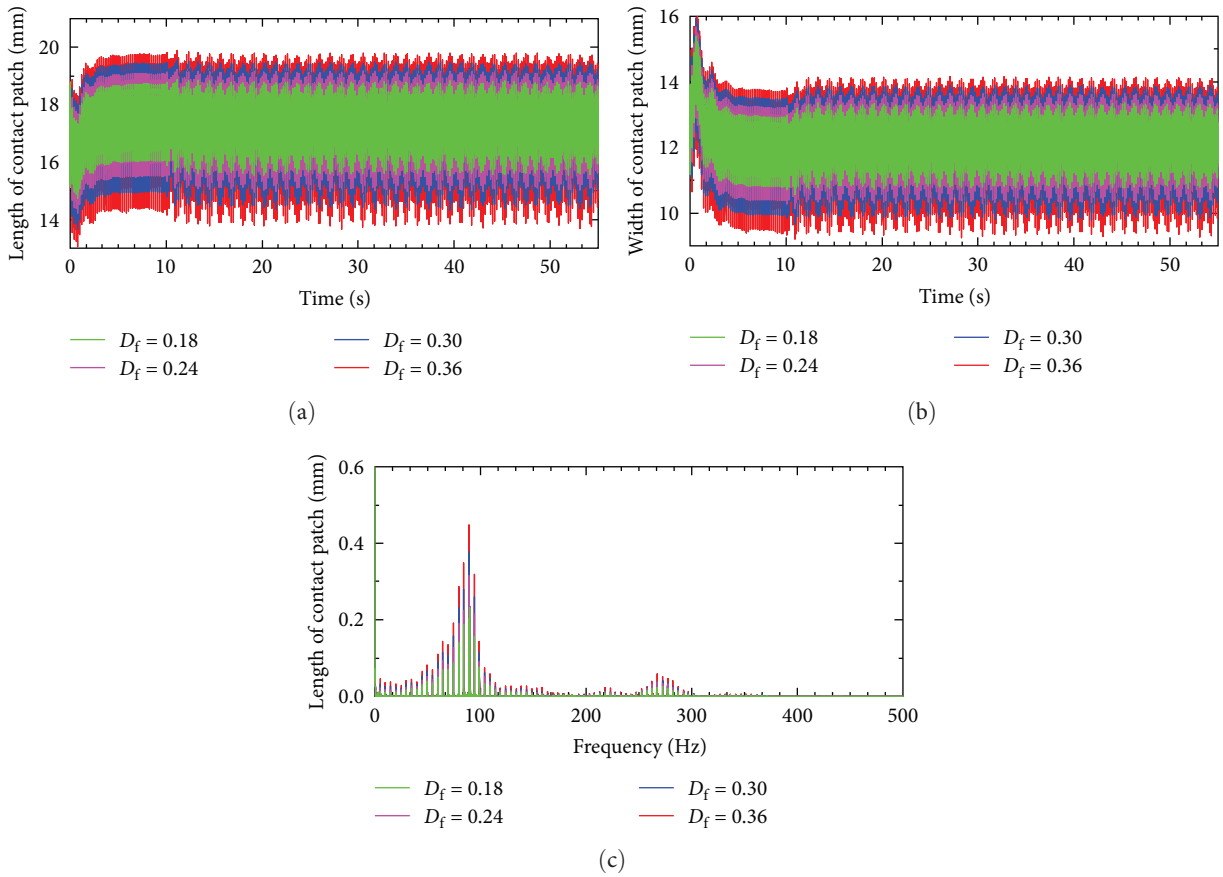

Figure 14: Size of contact patch: (a) length; (b) width; (c) FFT analysis of length.

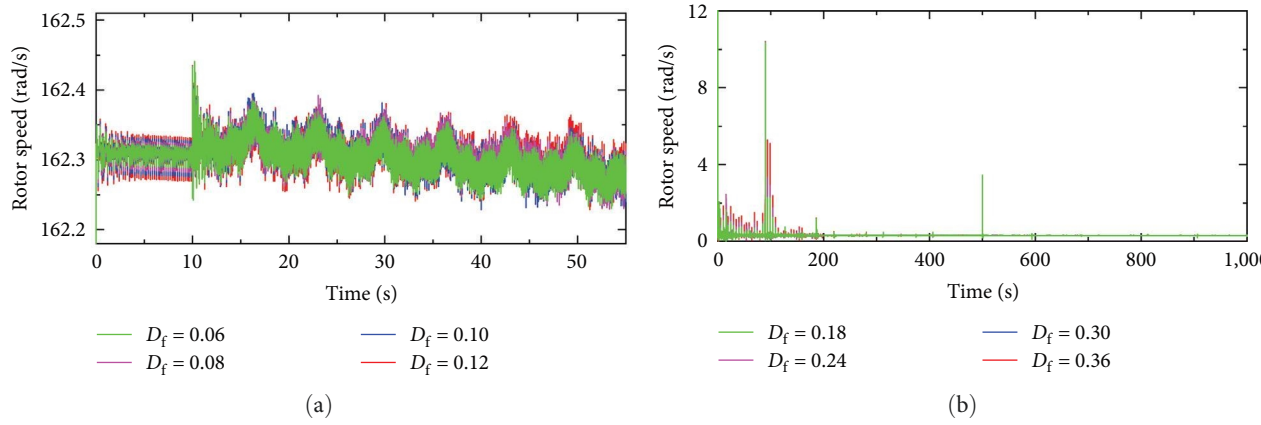

Figure 15: Rotor speed: (a) time history; (b) FFT analysis.

The motor torque from the electric traction drive system is shown in Figure 16. It can be seen that variations in the depth of the wheel flat have a minimal impact on the torque. As the depth of the wheel flat increases, the torque remains consistent in both the time domain and frequency domain. The transient current mentioned in Section 2.1 of the electric traction drive system, which is responsible for the inverter-motor. Field-oriented vector control is developed based on PI control. PI control has a certain degree of disturbance rejection capability. Therefore, despite the fluctuations in rotor speed feedback to the electric traction transmission system caused by the wheel flat depth variation, the motor torque output can remain unchanged.

4.2. The Impact of Wheel Flat Length on Traction Drive System. According to the simulation settings in Test 2, the electromechanical coupling model established in Section 3 was operated to obtain the mechanical and electrical parameters of the traction drive system. The temporal and spectral characteristics of the wheel-rail normal force are shown in Figure 17. When the flat length is 0.05 m, the vibration impact between the wheel and rail is exceptionally large. The minimum value of

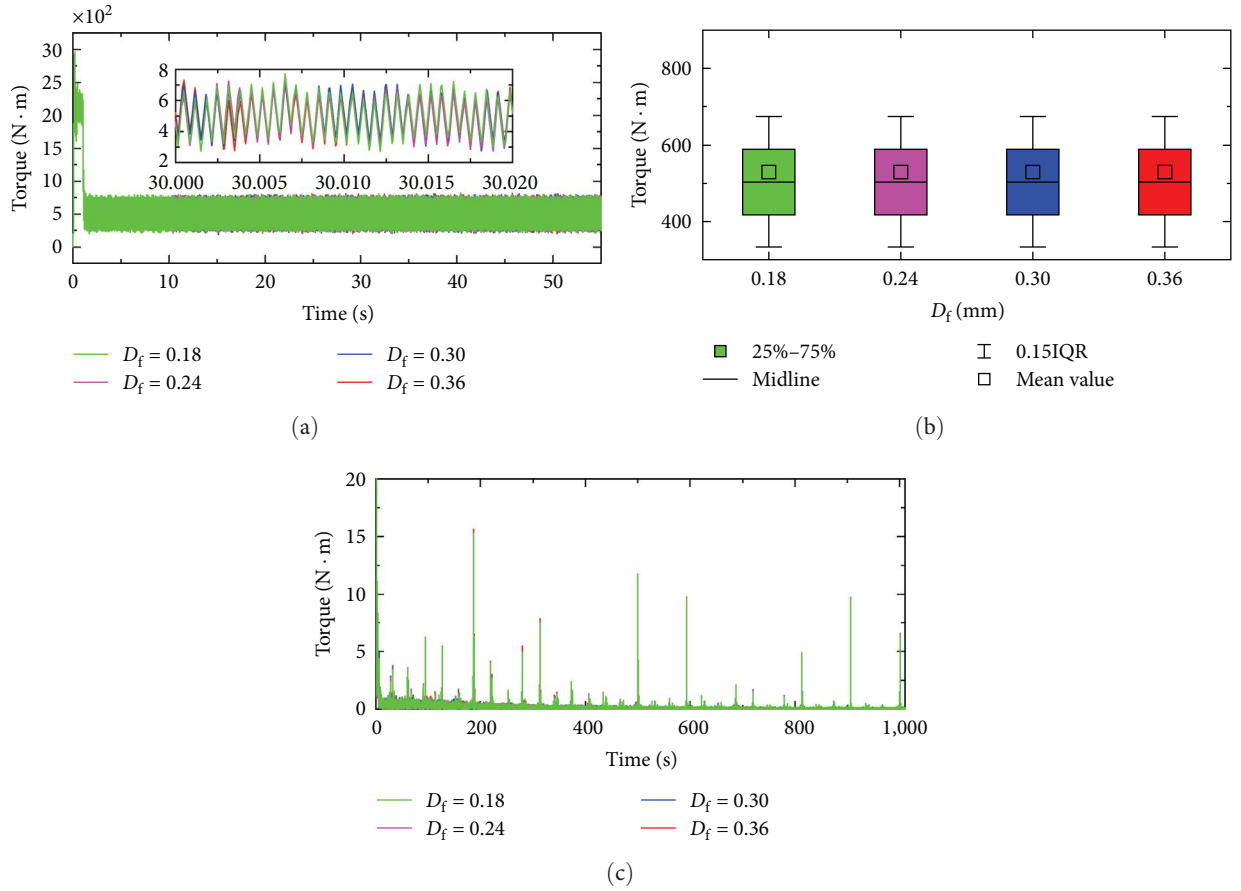

FIGURE 16: Torque: (a) time history; (b) box plot of torque; (c) FFT analysis.

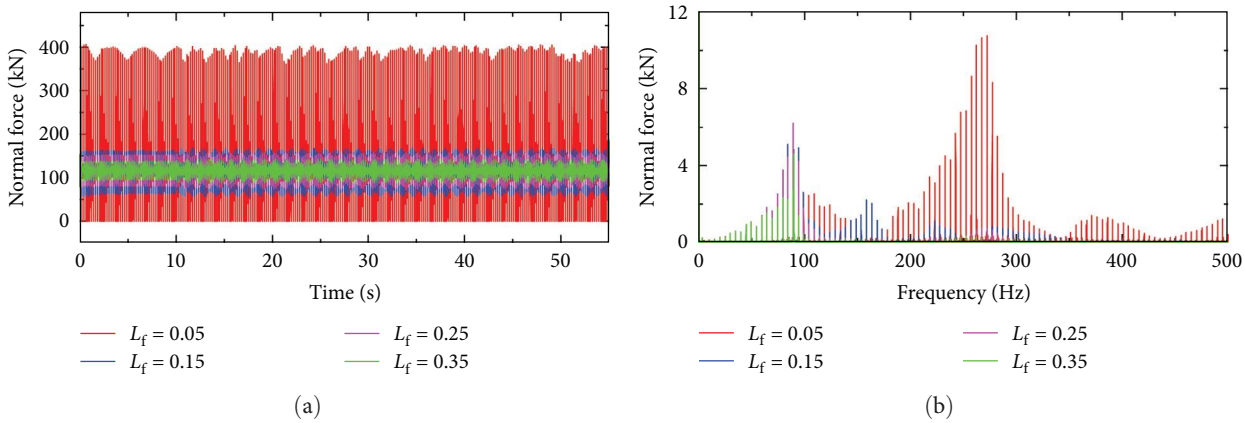

FIGURE 17: Wheel-rail normal force: (a) time history; (b) FFT analysis.

the normal force has already reached zero, indicating the occurrence of wheel-rail separation. It is worth noting that the spectral characteristics of the normal force at the flat length of 0.05 m are different from the other cases. In other cases, the frequency of the normal force fluctuation is mainly centered around 90 Hz. However, when $L_f = 0.05$ m, the frequency of the normal force fluctuation is mainly centered around 270 Hz, which is close to the second-order umbrella mode of the flexible wheelset (as can be seen in Figure 5). This indicates that the second-order umbrella mode of the wheelset is excited in this case. In Figure 18, it can be observed that as the wavelength of the flat decreases, the vibration impact of the normal force becomes more pronounced, and simultaneously, the rate of vibration attenuation slows down.

Figures 19–21 show the longitudinal creep, lateral creep, and spin creep of the wheel-rail contact. Overall, with the increase of the wheel flat length, the peak value of creepage fluctuation decreases. Except for the case with a flat length of 0.05 m, the fluctuation frequency of the longitudinal, lateral,

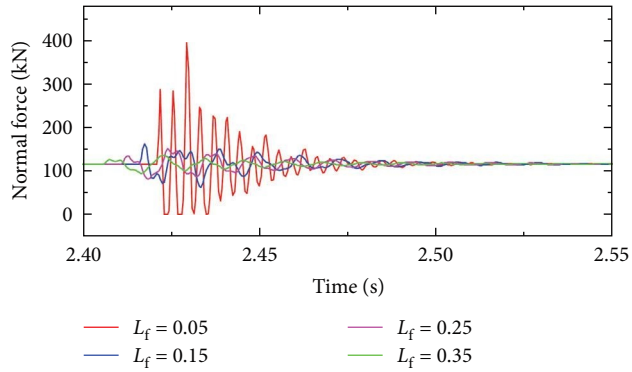

FIGURE 18: Magnified view of wheel normal force.

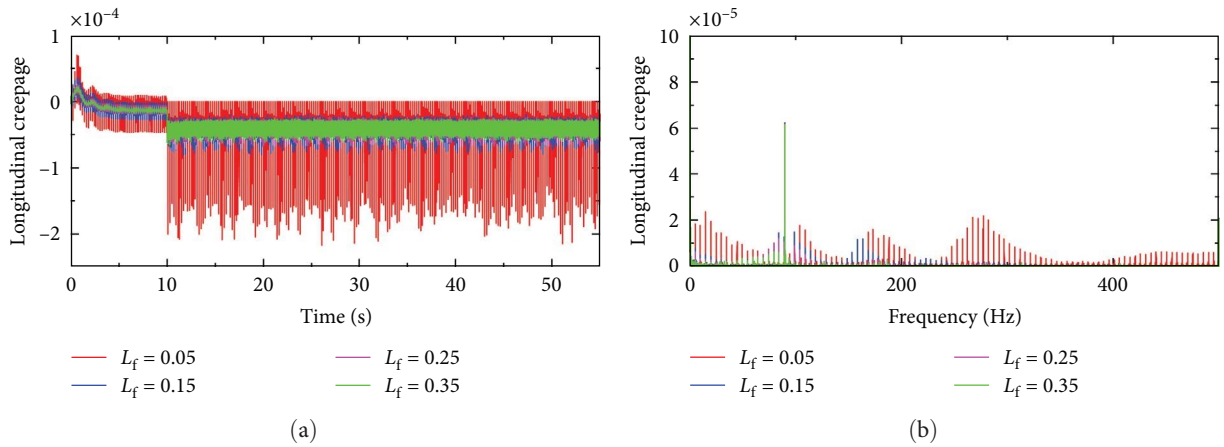

FIGURE 19: Longitudinal creepage: (a) time history; (b) FFT analysis.

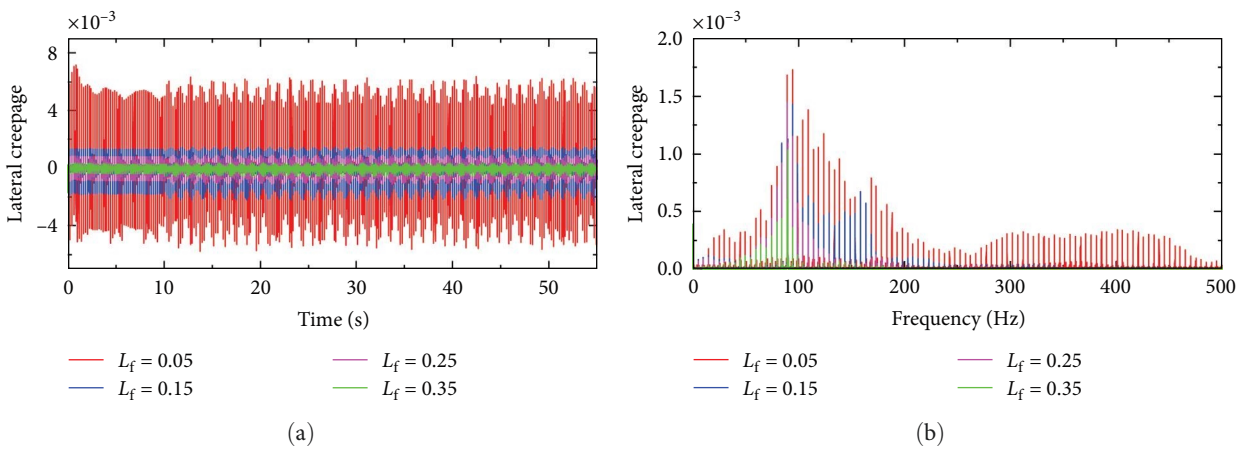

FIGURE 20: Lateral creepage: (a) time history; (b) FFT analysis.

and spin creep is mainly centered around 90 Hz. However, when $L_f = 0.05$ m, the fluctuation frequency of the spin creep is mainly centered around 275 Hz, but there is also a significant component at 90 Hz.

The temporal and spectral characteristics of the wheel-rail contact patch size are shown in Figure 22. Similar to the analysis in Section 4.1, the fluctuation characteristics of the contact patch size correspond to those in the normal force. As the flat length increases, the fluctuation of the contact patch size decreases. Except for the case with a flat length of 0.05 m, the fluctuation frequency is mainly centered around 90 Hz.

The temporal and spectral characteristics of the motor rotor angular velocity are shown in Figure 23. Except for the case with a flat length of 0.05 m, the fluctuation of the motor rotor speed is not sensitive to changes in the wheel flat length, and its main fluctuation frequency is mainly centered around 90 Hz. In the extreme case of $L_f = 0.05$ m, the rotor speed exhibits larger fluctuations, but it is important to note that its main fluctuation

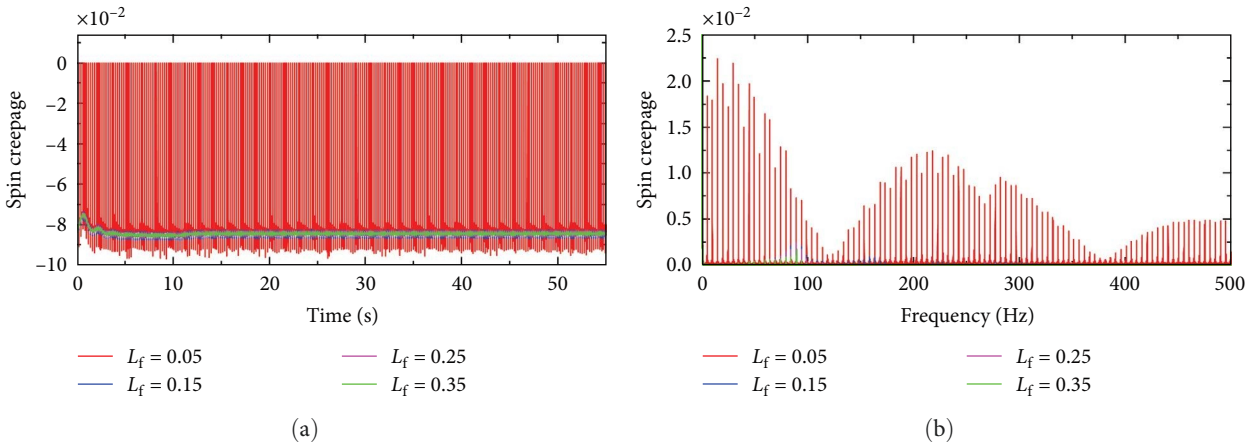

FIGURE 21: Spin creepage: (a) time history; (b) FFT analysis.

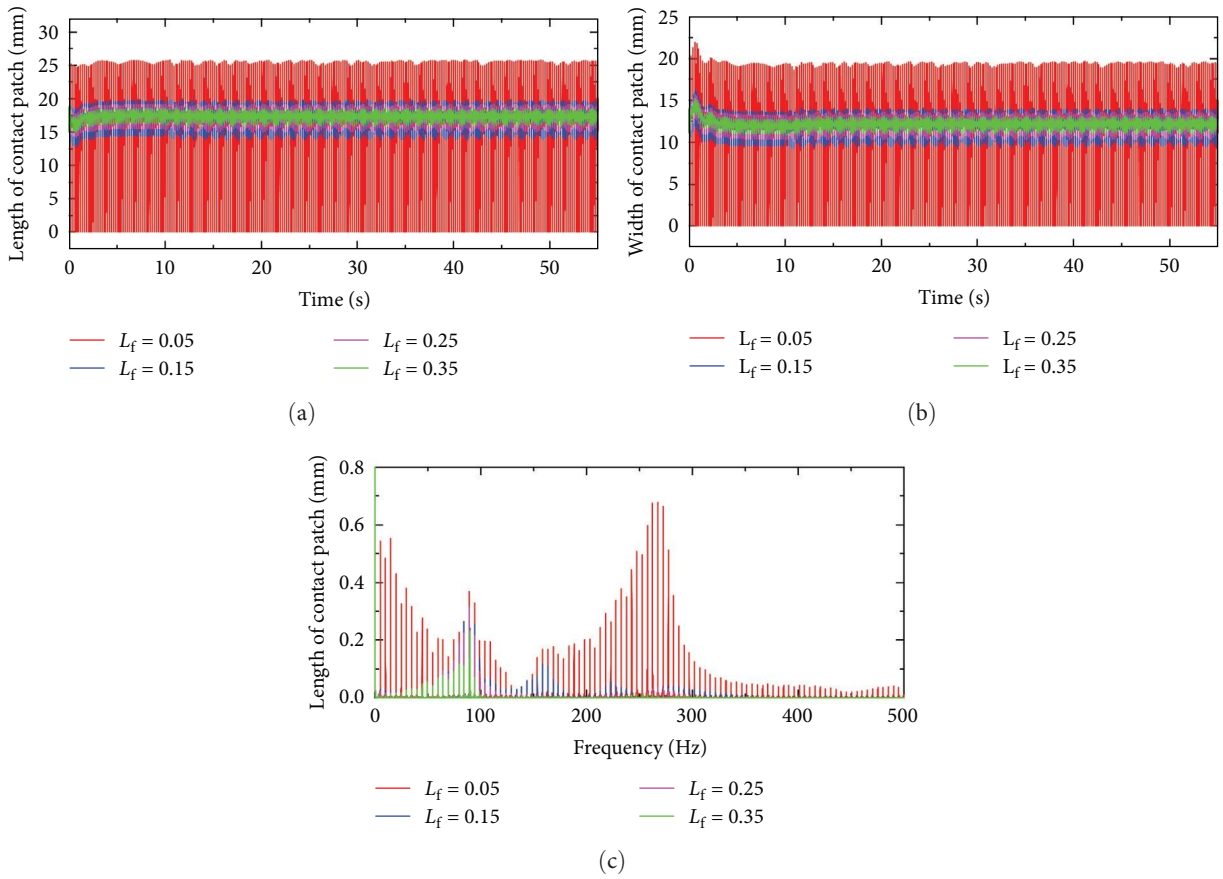

FIGURE 22: Size of contact patch: (a) length; (b) width; (c) FFT analysis of length.

frequency still remains centered around 90 Hz. Figure 24 presents the temporal and spectral characteristics of the motor torque. It can be seen that due to the anti-interference characteristics of the PI control, the motor output torque is not significantly affected by changes in the wheel flat depth.

4.3. Impact of Wheel Flats on the Traction Drive System at Different Speeds. Based on the simulation settings in Test 3, the electromechanical coupling model established in Part 3 is operated to obtain the mechanical and electrical parameters of the traction drive system. Figure 25 shows the wheel-rail normal force at the speed range of 60–100 km/hr. It can be observed that as the locomotive speed increases, the wheel flats can cause larger fluctuations in the normal force. From the spectral characteristics of the normal force in Figure 25(a), it can be seen that the main frequency of the fluctuation is around 90 Hz. However, it should be noted that as the locomotive speed increases, the components at 168 and 275 Hz gradually increase, which correspond to the first-order and second-order umbrella modes of the wheelset, as shown in

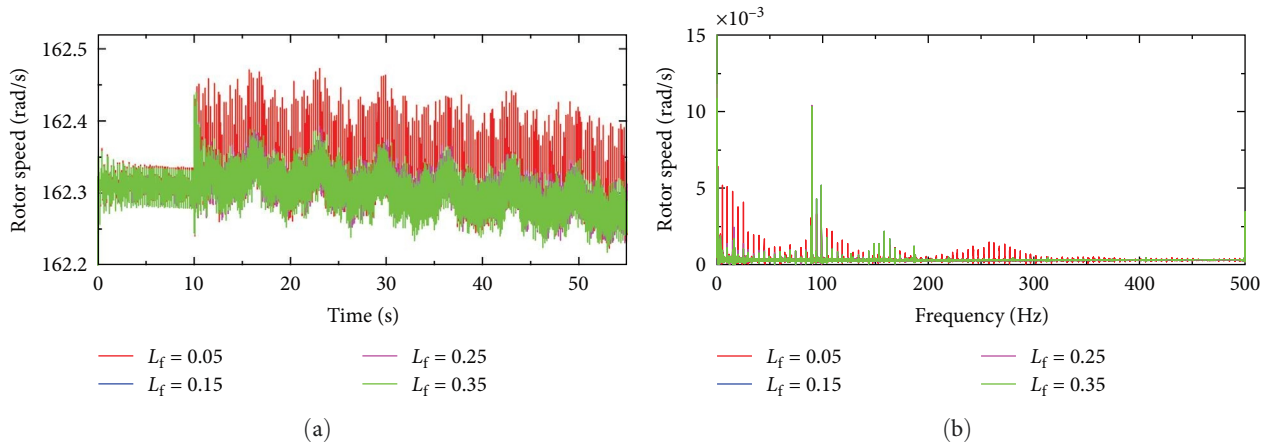

Figure 23: Rotor speed: (a) time history; (b) FFT analysis.

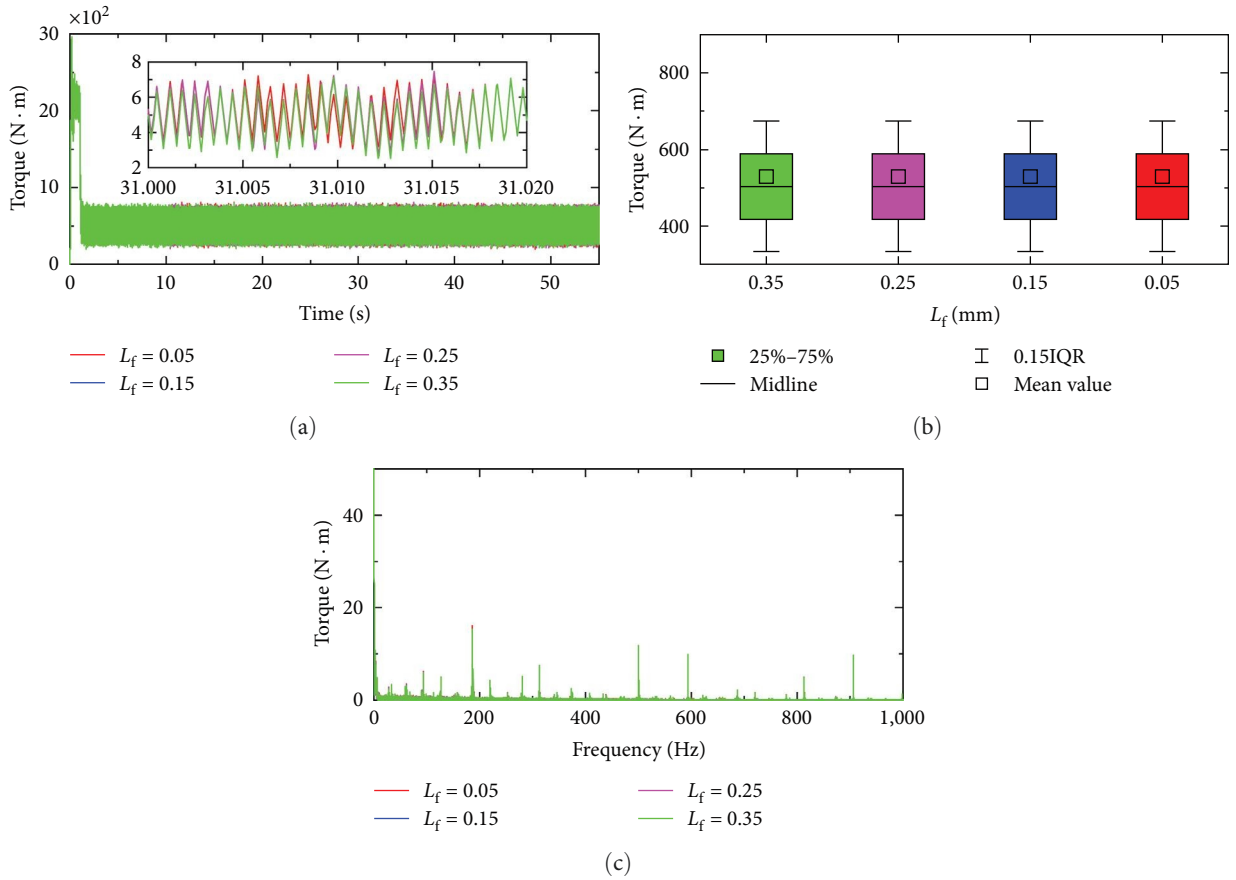

Figure 24: Torque: (a) time history; (b) box plot of toque; (c) FFT analysis.

Figure 2. Figure 26 shows the temporal characteristics of the wheel-rail normal force within the time span of 2.1–2.7 s at different speed levels. To clearly display the oscillation period of the normal force, we have shifted the normal force along the vertical axis for each speed. As the wheel rolling speed increases, the oscillation period of the normal force becomes shorter. This means that the normal force has not completely reached a steady state before the next impact occurs. This is the reason why the fluctuation of the normal force increases as the locomotive speed increases.

The longitudinal, lateral, and spin creepage of the wheel-rail contact at different speeds are shown in Figures 27–29. The longitudinal and lateral creepages are sensitive to changes in locomotive speed. As the locomotive speed increases, the fluctuations in the longitudinal and lateral creep coefficients become significantly larger. When the locomotive speed

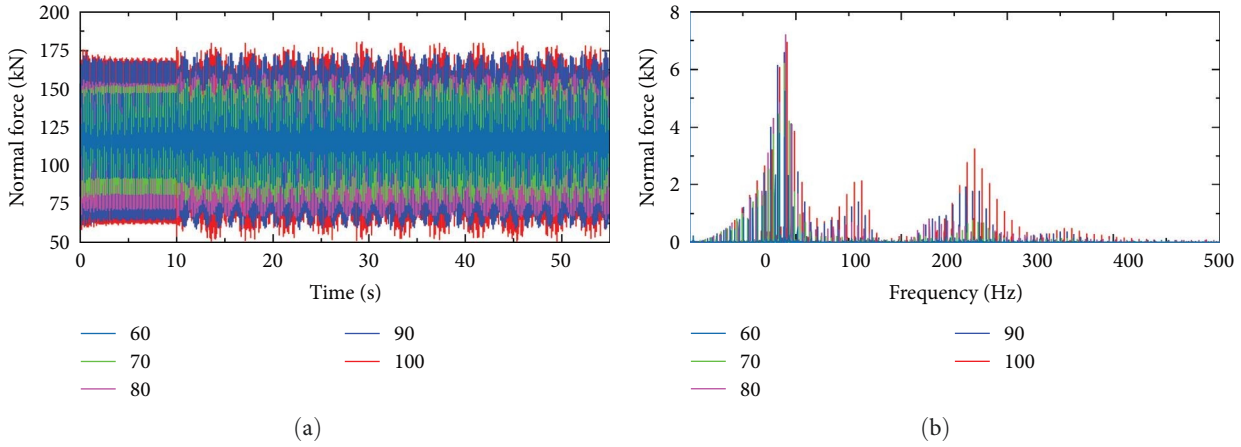

Figure 25: Wheel-rail normal force: (a) time history; (b) FFT analysis.

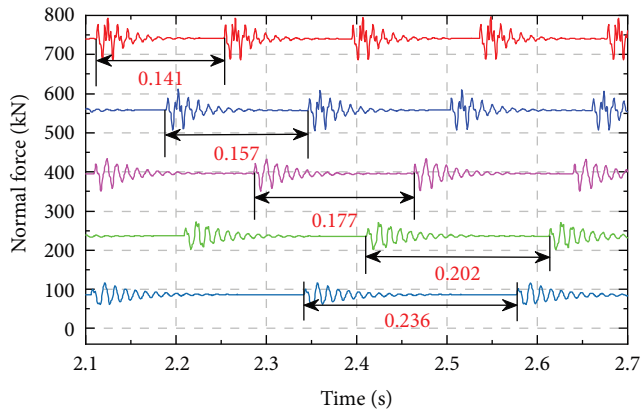

Figure 26: Magnified view of wheel normal force.

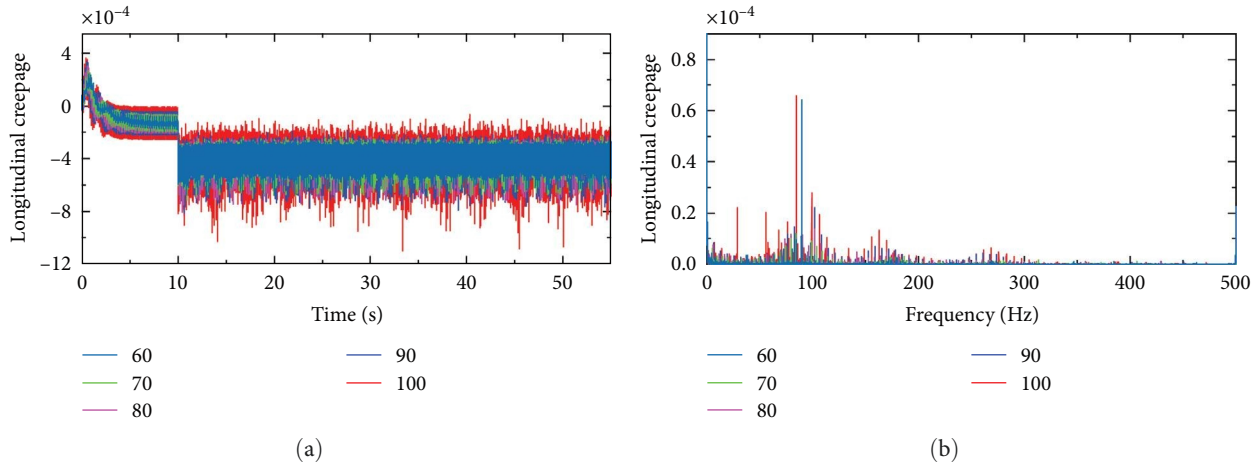

Figure 27: Longitudinal creepage: (a) time history; (b) FFT analysis.

reaches 100 km/hr, there is a significant spike in the longitudinal and lateral creepage. The main frequency component of the longitudinal and lateral creepage is 90 Hz. In Figure 29, as the running speed increases, the fluctuation of the spin creepage gradually increases, but it is slightly smaller than the longitudinal and lateral creepage. From Figure 29(b), it can be seen that there are significant components at 168 and 275 Hz in the spin creepage.

The temporal and spectral characteristics of the wheel-rail contact patch size are shown in Figure 30. The fluctuation of

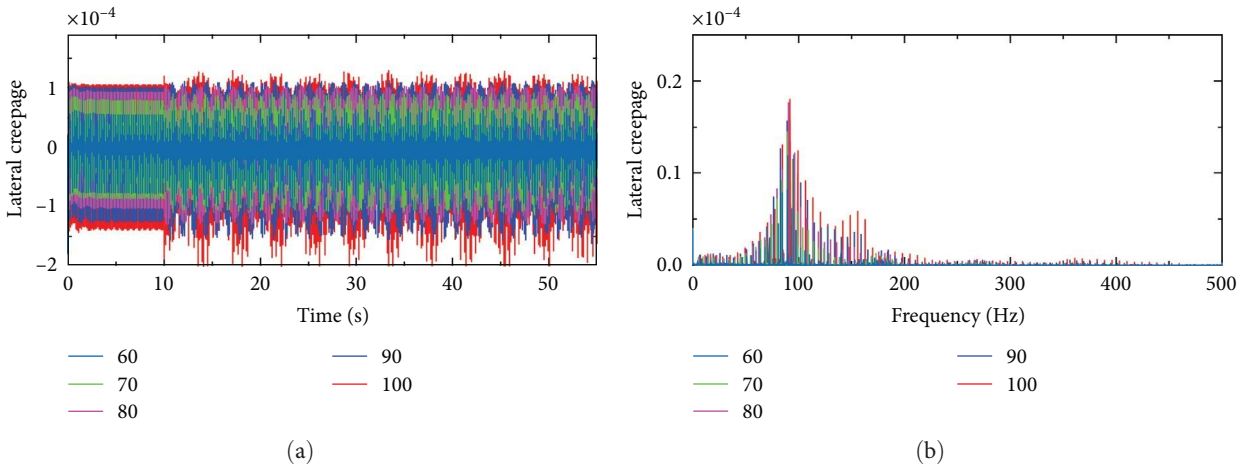

Figure 28: Lateral creepage: (a) time history; (b) FFT analysis.

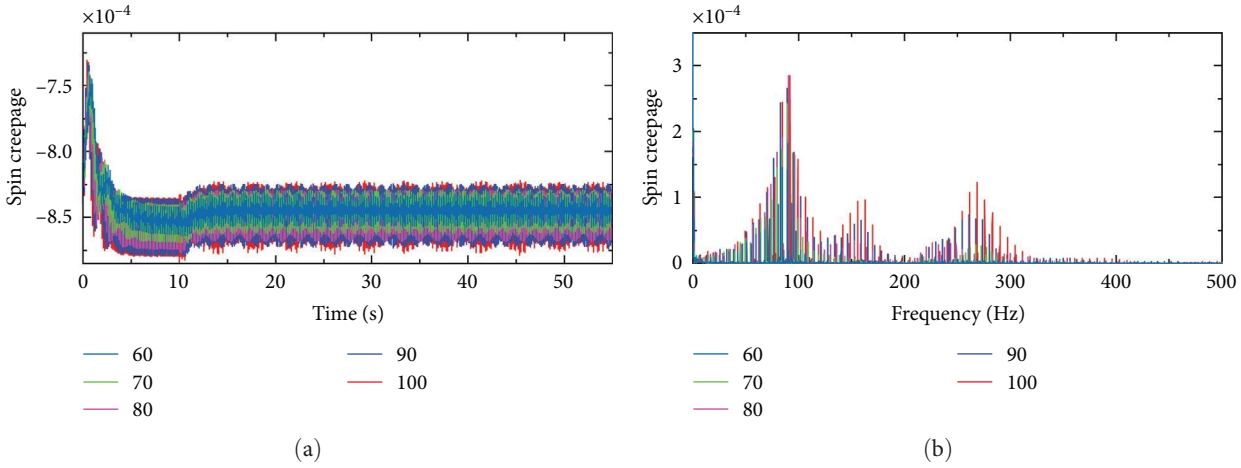

Figure 29: Spin creepage: (a) time history; (b) FFT analysis.

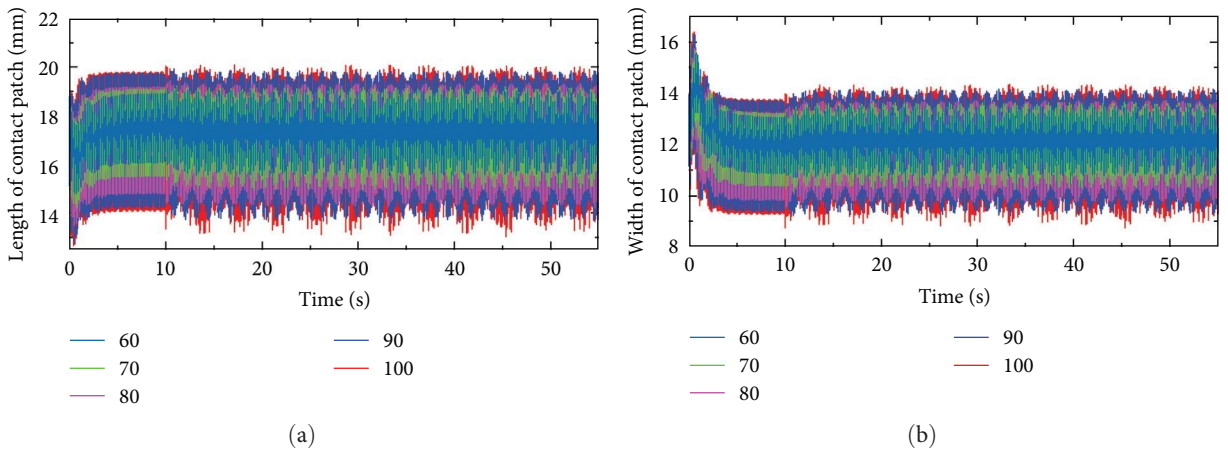

Figure 30: Continued.

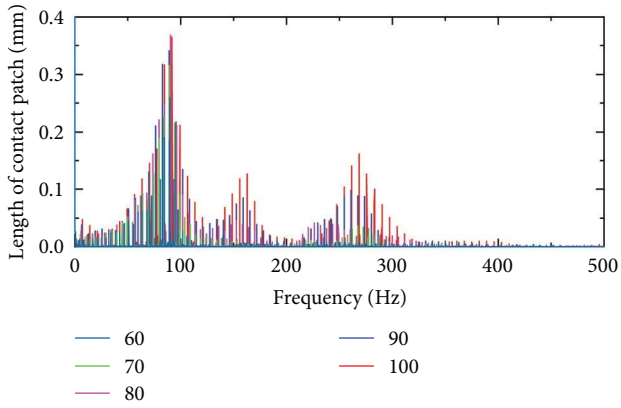

(c)

Figure 30: Size of contact patch: (a) length; (b) width; (c) FFT analysis of length.

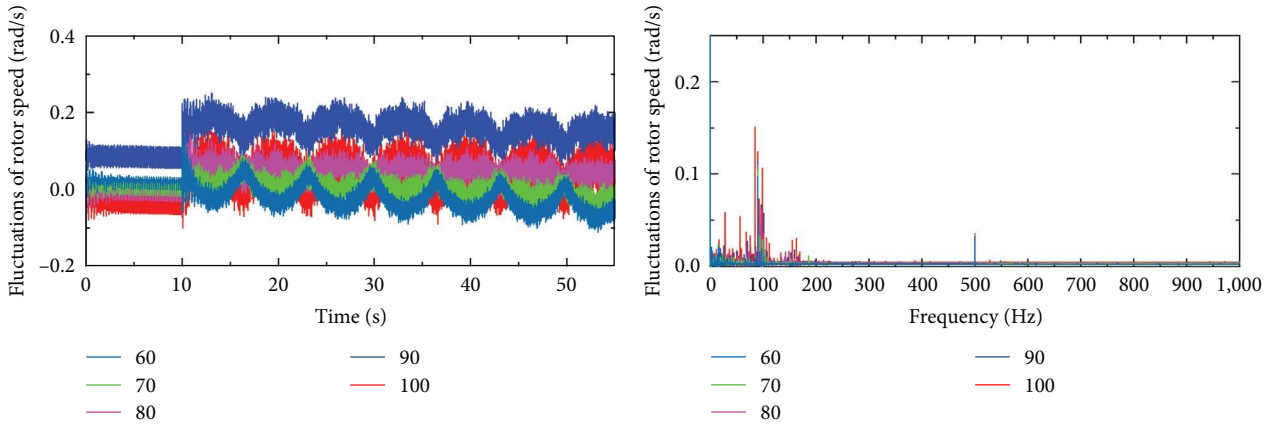

(a) (b)

Figure 31: Fluctuations of rotor speed: (a) time history; (b) FFT analysis.

the contact patch size increases with the locomotive speed. From Figure 30(b), it can be seen that the fluctuation of the contact patch size contains components at 90, 168, and 275 Hz, which is similar to the normal force. As the locomotive operates at different speeds, the rotor speed of the motor also varies. To compare the rotor fluctuations at different speeds more clearly, the measured rotor speed waveform is subtracted by its mean value, as shown in Figure 31. The rotor speed fluctuations are not sensitive to changes in locomotive speed. When the locomotive speed increases from the range of 60 to 90 km/hr, the rotor speed fluctuations remain relatively unchanged. However, when the locomotive operates at 100 km/hr, there is a significant increase in rotor speed fluctuations. The fluctuation frequency of the rotor speed is mainly centered around 90 Hz.

Since the resistance experienced by the locomotive is related to the running speed, the required traction torque output from the motor varies at different speed levels. To depict the variation in torque fluctuations more clearly, the waveform of the motor output torque at different running speeds is subtracted by its mean value, as shown in Figure 32. When the locomotive operates in the range of 60–90 km/hr, the torque fluctuations slowly increase with the locomotive speed. However, when the locomotive speed reaches 100 km/hr, there is a significant increase in torque fluctuations. It is worth noting that there are distinct differences in torque fluctuations before and after applying torque excitations. The torque mainly contains fluctuations at 90 Hz.

5. Conclusions

Based on the electromechanical coupling system of the electric traction drive system and the locomotive-track coupling dynamics system, this study investigated the impact of wheel flats on the locomotive traction drive system. The following important conclusions can be drawn:

(1) Wheel flats can excite the first-order bending mode of the wheel-rail system, leading to significant fluctuations in the dynamic responses of the wheel-rail system and rotor speed, primarily at a frequency of 90 Hz.

(2) The wheel-rail normal force, creepage, and contact patch area are significantly influenced by changes in

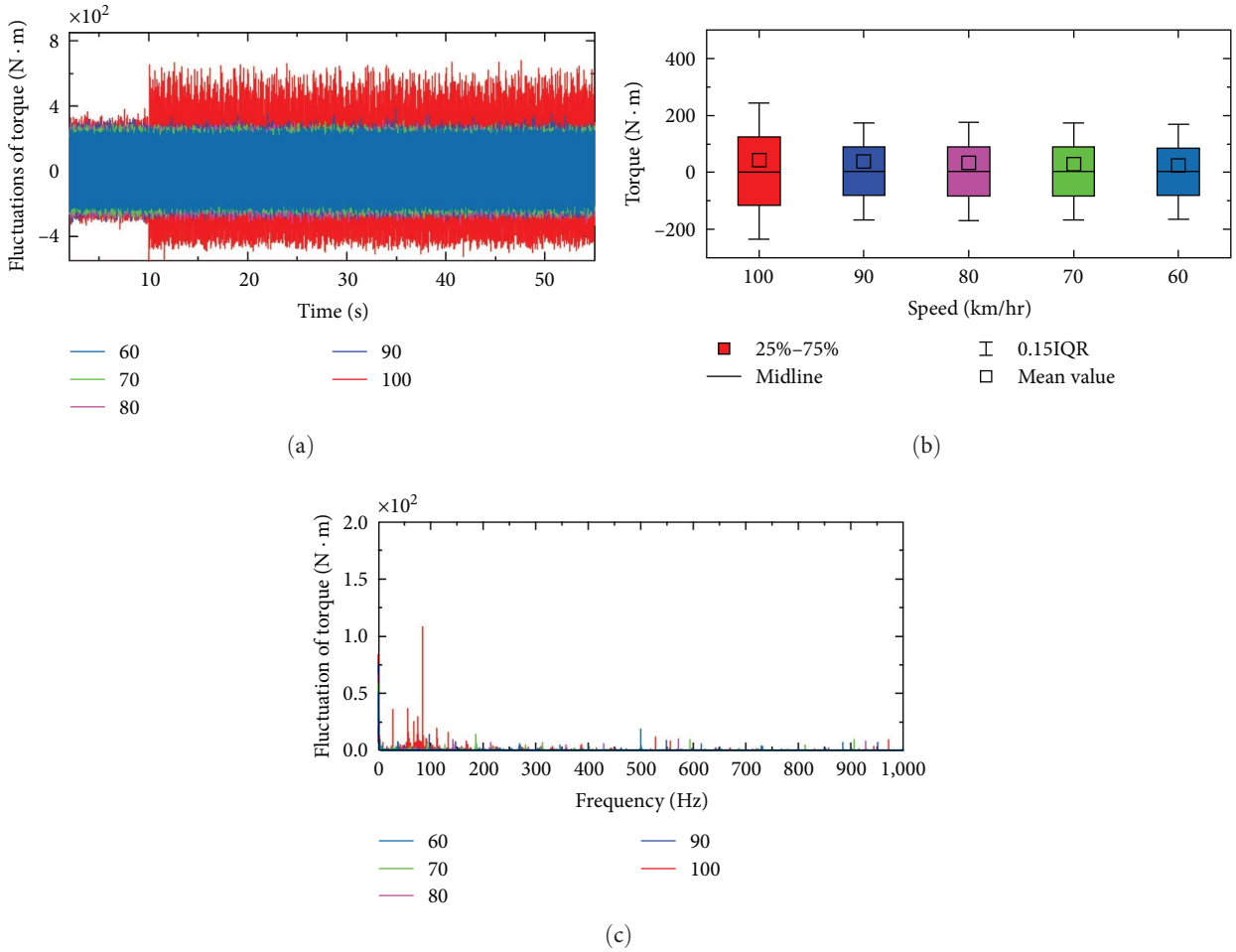

FIGURE 32: Torque: (a) time history; (b) box plot of toque; (c) FFT analysis.

the depth of wheel flats. As the depth of the flats increases, the magnitude of these parameters' fluctuations also increases. However, the rotor speed and torque are not significantly affected by changes in the depth of wheel flats.

(3) The wheel-rail normal force, creepage, contact patch area, and rotor speed are sensitive to changes in the length of wheel flats. Smaller flat lengths result in larger fluctuations in these parameters. Again, the torque is not significantly affected by changes in the length of wheel flats. When the flat length reaches 0.05 m, the wheel-rail system experiences severe vibrations, leading to wheel-rail separation.

(4) With increasing locomotive speed, the impact of wheel flats on electrical and mechanical parameters becomes more significant. When the locomotive speed reaches 100 km/hr, there is a noticeable increase in torque fluctuations.

Data Availability

Data will be available upon reasonable request.

Conflicts of Interest

The authors declare that they have no conflicts of interest.

Acknowledgments

This work was supported in part by the Natural Science Foundation Project of Sichuan Province (24NSFSC7248), National Natural Science Foundation of China (52172408), Science and Technology Research and Development Project of China National Railway Group Co., Ltd. (N2023T011-A (JB)), Research Project of China Academy of Railway Sciences Group Co., Ltd. (2023YJ277), and the open project of State Key Laboratory of Traction Power (no. TPL2211).

References

[1] G. Tao, L. Wang, Z. Wen, Q. Guan, and X. Jin, "Measurement and assessment of out-of-round electric locomotive wheels," *Proceedings of the Institution of Mechanical Engineers, Part F: Journal of Rail and Rapid Transit*, vol. 232, no. 1, pp. 275–287, 2018.

[2] W. Liu, N. Yan, Q. Pu, and L. Wang, "Development trend of wheelset polygon on type HXD1 locomotive," *Electric*

Locomotives and Urban Rail Vehicles, vol. 40, no. 6, pp. 55–59, 2017.

[3] B. Lu, Y. Song, Z. Liu et al., "Evolution analysis of wheel polygon wear considering the effect of interharmonics in electrical traction drive system," *Mechanism and Machine Theory*, vol. 191, Article ID 105470, 2024.

[4] Z. Chen, H. Lin, L. Yao, J. Yang, and Z. Li, "Dynamic response of wheel-rail under tread flat load of wheel on high-speed railway," *High Speed Railway Technology*, vol. 13, no. 4, pp. 47–57, 2022.

[5] G. Tao, *Investigation into the Formation Mechanism of the Polygonal Wear of HXD Electric Locomotive Wheels [dissertation]*, Southwest Jiaotong University, Chengdu, Chengdu, 2018.

[6] A. Mosleh, A. Meixedo, D. Ribeiro, P. Montenegro, and R. Calçada, "Early wheel flat detection: an automatic data-driven wavelet-based approach for railways," *Vehicle System Dynamics*, vol. 61, no. 6, pp. 1644–1673, 2023.

[7] A. Mosleh, A. Meixedo, D. Ribeiro, P. Montenegro, and R. Calçada, "Automatic clustering-based approach for train wheels condition monitoring," *International Journal of Rail Transportation*, vol. 11, no. 5, pp. 639–664, 2023.

[8] J. Wang, P. Wu, and Z. Zhao, "Research on the axle stress spectrum considering extra wheel flat impact forces," *Journal of the China Railway Society*, vol. 1, pp. 39–43, 2006.

[9] R. U. A. Uzzal, W. Ahmed, and S. Rakheja, "Dynamic analysis of pitch plane railway vehicle-track interactions due to single and multiple wheel flats," in *Proceedings of the IEEE/ASME/ASCE 2008 Joint Rail Conference. IEEE/ASME/ASCE 2008 Joint Rail Conference*, ASME, Wilmington, Delaware, USA, April 2008.

[10] R. U. A. Uzzal, A. K. W. Ahmed, and R. B. Bhat, "Modelling, validation and analysis of a three-dimensional railway vehicle–track system model with linear and nonlinear track properties in the presence of wheel flats," *Vehicle System Dynamics*, vol. 51, no. 11, pp. 1695–1721, 2013.

[11] J. Yang and D. Thompson, "Wheel flat impact noise prediction using detailed contact model," in *Proceedings of Acoustics 2012 Nantes Conference*, Acoustics 2012, Nantes, France, 2012.

[12] L. Baeza, A. Roda, J. Carballeira, and E. Giner, "Railway train-track dynamics for wheelflats with improved contact models," *Nonlinear Dynamics*, vol. 45, pp. 385–397, 2006.

[13] C. Chang, Y. Cai, B. Chen, Q. Li, and P. Lin, "Experimental study of the wheel/rail impact caused by wheel flat within 400 km/h using full-scale roller rig," *Railway Sciences*, vol. 1, no. 1, pp. 76–89, 2022.

[14] Y. Liu, J. X. Liu, and Y. J. Guo, "Study on dynamic simulation input form of locomotive wheel flat," *Applied Mechanics and Materials*, vol. 215-216, pp. 946–949, 2012.

[15] F. Lin, R. Wang, Y. Yang, Q. Xiao, Z. Xu, and X. Dong, "Analysis of the impact of wheel flat scars on wheel rail impact," *Machine Tool and Hydraulics*, vol. 49, no. 3, pp. 140–144, 2021.

[16] D. Zhang, K. Wang, and W. Zhai, "Effect of wheel flats on wheel/rail dynamic interaction in 30-ton heavy-haul railway," *Journal of Southwest University of Science and Technology*, vol. 30, no. 4, pp. 15–19, 2015.

[17] L. Han, L. Jing, and L. Zhao, "Finite element analysis of the wheel–rail impact behavior induced by a wheel flat for high-speed trains: the influence of strain rate," *Proceedings of the Institution of Mechanical Engineers, Part F: Journal of Rail and Rapid Transit*, vol. 232, no. 4, pp. 990–1004, 2017.

[18] Z. Ren, "An investigation on wheel/rail impact dynamics with a three-dimensional flat model," *Vehicle System Dynamics*, vol. 57, no. 3, pp. 369–388, 2019.

[19] L. Han, L. Jing, and K. Liu, "A dynamic simulation of the wheel–rail impact caused by a wheel flat using a 3-D rolling contact model," *Journal of Modern Transportation*, vol. 25, pp. 124–131, 2017.

[20] Z. Wang, L. Zhang, Z. Ren, J. Mo, L. Yang, and K. Wang, "Friction and vibration behaviours of high-speed train brake system excited by wheel flats," *International Journal of Rail Transportation*, pp. 1–18, 2023.

[21] Y. Ye, D. Shi, P. Krause, Q. Tian, and M. Hecht, "Wheel flat can cause or exacerbate wheel polygonization," *Vehicle System Dynamics*, vol. 58, no. 10, pp. 1575–1604, 2020.

[22] J. Yang, Y. Zhao, J. Wang, C. Liu, and Y. Bai, "Influence of wheel flat on railway vehicle helical gear system under Traction/Braking conditions," *Engineering Failure Analysis*, vol. 134, Article ID 106022, 2022.

[23] Z. Wang, Y. Cheng, G. Mei, W. Zhang, G. Huang, and Z. Yin, "Torsional vibration analysis of the gear transmission system of high-speed trains with wheel defects," *Proceedings of the Institution of Mechanical Engineers, Part F: Journal of Rail and Rapid Transit*, vol. 234, no. 2, pp. 123–133, 2020.

[24] T. Zhang, Z. Chen, W. Zhai, K. Wang, and Z. Li, "Dynamic performance of gear transmission systemin a heavy-haul locomotive under wheel flat impact," *Chinese Science Bulletin*, vol. 64, no. 25, pp. 2566–2572, 2019.

[25] B. Guo, Z. Luo, B. Zhang, Y. Liu, and Z. Chen, "Dynamic influence of wheel flat on fatigue life of the traction motor bearing in vibration environment of a locomotive," *Energies*, vol. 14, no. 18, Article ID 5810, 2021.

[26] Y. Jianwei, Y. Zhao, J. Wang, Y. Bai, and C. Liu, "Investigation on impact response feature of railway vehicles with wheel flat fault under variable speed conditions," *Journal of Vibration and Acoustics*, vol. 142, no. 3, Article ID 031009, 2020.

[27] W. Zhai, *Vehicle-Track Coupled Dynamics*, Springer, Singapore, 2020.

[28] Y. Yang, F. Chai, P. Liu, L. Ling, K. Wang, and W. Zhai, "On the polygonal wear evolution of heavy-haul locomotive wheels due to wheel/rail flexibility and its mitigation measures," *Chinese Journal of Mechanical Engineering*, vol. 37, Article ID 16, 2024.

[29] X. Jin and Q. Liu, *Wheel-Rail Tribology*, China Railway Press, Beijing, Chinese, 2004.

[30] M. S. Sichani, R. Enblom, and M. Berg, "An alternative to FASTSIM for tangential solution of the wheel–rail contact," *Vehicle System Dynamics*, vol. 54, no. 6, pp. 748–764, 2016.

[31] J. J. Kalker, "A fast algorithm for the simplified theory of rolling contact," *Vehicle System Dynamics*, vol. 11, no. 1, pp. 1–13, 1982.

[32] R. Enblom and M. Berg, "Simulation of railway wheel profile development due to wear—influence of disc braking and contact environment," *Wear*, vol. 258, no. 7-8, pp. 1055–1063, 2005.

[33] X. Feng, *Electric Traction AC Drive and Its Control System*, Higher Education Press, Beijing, Chinese, 2009.

[34] Z. Li, H. Lei, and Y. Zhu, "Analysis of rayleigh damping parameters in a dynamic system of vehicle-track-bridge," *Journal of Vibration and Shock*, vol. 32, no. 21, pp. 52–57+73, 2013.

[35] P. Dey, P. Kirawanich, C. Sumpavakup, and A. Bhattacharya, "Tuning of controller parameters for suppressing low frequency oscillationsin electric railway traction networks using meta-heuristic algorithms," *IET Electrical System Transporation*, vol. 13, no. 2, Article ID e12075, 2023.

[36] Y. Song, H. Wang, G. Frøseth, P. Nåvik, Z. Liu, and A. Rønnquist, "Surrogate modelling of railway pantograph-

catenary interaction using deep long-short-term-memory neural networks," *Mechanism and Machine Theory*, vol. 187, Article ID 105386, 2023.

[37] F. Duan, Y. Song, S. Gao et al., "Study on aerodynamic instability and galloping response of rail overhead contact line based on wind tunnel tests," *IEEE Transactions on Vehicular Technology*, vol. 72, no. 6, pp. 7211–7220, 2023.

[38] Y. Song, X. Lu, Y. Yin, Y. Liu, and Z. Liu, "Optimization of railway pantograph-catenary systems for over 350 km/h based on an experimentally validated model," *IEEE Transactions on Industrial Informatics*, pp. 1–11, 2024.

[39] X. Meng, Z. Liu, G. Li, X. Chen, S. Wu, and K. Hu, "A multi-frequency input-admittance model of locomotive rectifier considering PWM sideband harmonic coupling in electrical railways," *IEEE Transactions on Transportation Electrification*, vol. 8, no. 3, pp. 3848–3858, 2022.

[40] Z. Liu, Y. Song, S. Gao, and H. Wang, "Review of perspectives on pantograph-catenary interaction research for high-speed railways operating at 400 km/h and above," *IEEE Transactions on Transportation Electrification*, 2023.

[41] B. Lu, Z. Liu, X. Wang et al., "Influence of electric traction drive system harmonics and interharmonics on the vibration of key locomotive components," *IEEE Transactions on Vehicular Technology*, vol. 72, no. 10, pp. 12830–12844, 2023.

[42] Y. Song, A. Rønnquist, T. Jiang, and P. Nåvik, "Railway pantograph-catenary interaction performance in an overlap section: modelling, validation and analysis," *Journal of Sound and Vibration*, vol. 548, Article ID 117506, 2023.

[43] X. Wang, Z. Liu, Y. Song et al., "Dynamic characteristics of electric shoegear and conductor rail system considering the track irregularities," *IEEE Transactions on Instrumentation and Measurement*, vol. 72, pp. 1–13, 2023.

[44] Y. Song, Z. Liu, A. Rønnquist, P. Nåvik, and Z. Liu, "Contact wire irregularity stochastics and effect on high-speed railway pantograph-catenary interactions," *IEEE Transactions on Instrumentation and Measurement*, vol. 69, no. 10, pp. 8196–8206, 2020.

[45] Y. Song, Z. Wang, Z. Liu, and R. Wang, "A spatial coupling model to study dynamic performance of pantograph-catenary with vehicle-track excitation," *Mechanical Systems and Signal Processing*, vol. 151, Article ID 107336, 2021.

[46] R. Menon, N. A. Azeez, A. H. Kadam, and S. S. Williamson, "Study and analysis of the effects of varied PWM techniques and power sharing ratios on the current ripple in open-ended, three-level traction motor drives," *IET Electrical Systems in Transportation*, vol. 10, no. 2, pp. 154–161, 2020.

[47] M. Shafighy, S. Khoo, and A. Z. Kouzani, "Modelling and simulation of regeneration in AC traction propulsion system of electrified railway," *IET Electrical Systems in Transportation*, vol. 5, no. 4, pp. 145–155, 2015.

[48] Y. Luo, J. Yao, Z. Chen et al., "Transient synchronous stability analysis and enhancement control strategy of a PLL-based VSC system during asymmetric grid faults," *Protection and Control of Modern Power Systems*, vol. 8, Article ID 35, 2023.

[49] Q. Zhang, Y. Zhang, K. Huang et al., "Modeling of regenerative braking energy for electric multiple units passing long downhill section," *IEEE Transactions on Transportation Electrification*, vol. 8, no. 3, pp. 3742–3758, 2022.

[50] X. Meng, Z. Liu, Y. Liu et al., "Conversion and SISO equivalence of impedance model of single-phase converter in electric multiple units," *IEEE Transactions on Transportation Electrification*, vol. 9, no. 1, pp. 1363–1378, 2023.

[51] W. Song and X. Feng, *Control and Modulation Technologies of Electric AC Drives*, Science Press, Beijing, Chinese, 2014.

[52] S. Zhou, M. Zhu, J. Lin, P. G. Ipoum-Ngome, D. L. Mon-Nzongo, and T. Jin, "Discrete space vector modulation and optimized switching sequence model predictive control for three-level voltage source inverters," *Protection and Control of Modern Power Systems*, vol. 8, Article ID 64, 2023.

[53] Y. Fan, D. Hu, W. Chen et al., "Harmonic feature of 27.5 kV traction power system in a Chinese high-speed railway," *IET Electrical Systems in Transportation*, vol. 12, no. 4, pp. 369–379, 2022.

[54] A. Mariscotti, "Experimental characterisation of active and non-active harmonic power flow of AC rolling stock and interaction with the supply network," *IET Electrical Systems in Transportation*, vol. 11, no. 2, pp. 109–120, 2021.

[55] N. Zhao, J. Zhang, Z. Mao, Z. Jiang, and H. Li, "Time-frequency feature extraction method of the multi-source shock signal based on improved VMD and bilateral adaptive laplace wavelet," *Chinese Journal of Mechanical Engineering*, vol. 36, Article ID 36, 2023.